Journal of Materials Chemistry A

Accepted Manuscript

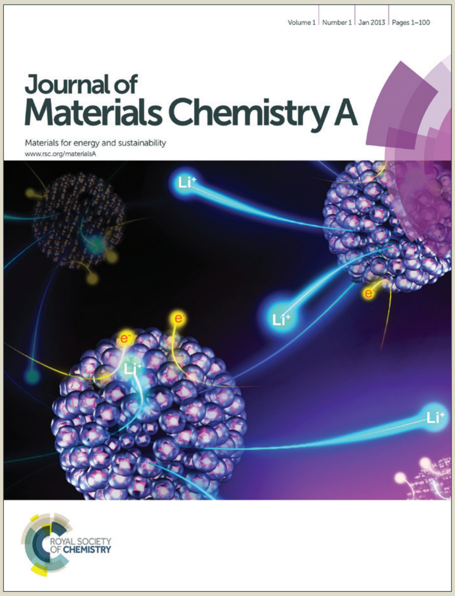

ROYAL SOCIETY OF CHEMISTRY

www.rsc.org/materialsA

Journal of Materials Chemistry A RSCPublishing

ARTICLE

Cite this: DOI: 10.1039/x0xx00000x

Received 00th January 2012,
Accepted 00th January 2012

DOI: 10.1039/x0xx00000x

www.rsc.org/

Sustainable activated carbon fibers from liquefied wood with controllable porosity for high-performance supercapacitors

Zhi Jin,†[a] Xiaodong Yan,†[b] Yunhua Yu,*[b] Guangjie Zhao*[a]

Activated carbons are regarded as the most important electrode materials for commercial supercapacitors because of their low cost, high surface area, and good electrical conductivity. The environmentally-friendly, low-cost and renewable biomass is a promising raw material for high-performance carbon electrode material. Herein, a series of activated carbon fibers (ACFs) are fabricated by one-step carbonization and activation of wood-derived fibers with different activation time. The micropore surface area, mesopore/micropore ratio and pore size of the ACFs series are successfully controlled by adjusting the levels of burn-off in order to study the effects of these parameters on specific capacitance and rate capability. Electrochemical measurements show that the electrochemical performance of the ACFs series increases with the progress of gasification unless excessive burn-off occurs. The sample with optimal structure exhibits an outstanding specific capacitance of 280 F g^{-1} at 0.5 A g^{-1} and excellent rate capability (81.8% capacitance retention at 10 A g^{-1}) in 1 M H_2SO_4. Furthermore, it demonstrates good cyclic stability, showing high capacitance retention of 99.3% over 2000 charge/discharge cycles. The excellent electrochemical performance of this sample is attributed to the large micropore surface area, a proportion of mesopores in the range of 3–4 nm, good electrical conductivity and fast charge transfer.

1 Introduction

Electric double-layer capacitors, also known as supercapacitors, present higher power density and much longer cycle life as compared to batteries due to the different nature of energy storage.[1] Electric double-layer capacitors store energy through rapid and reversible adsorption of electrolyte ions onto the surface of the electrodes, generally made from porous carbons which possess high surface area, good electrical conductivity and high physicochemical stability.[2-4] Activated carbons have been commercially used as supercapacitor electrode materials for several decades because of their lower cost compared with other porous carbons (e.g. templated carbons and carbide-derived carbons), and still will be the most widely used electrode materials in the next few decades. However, commercial activated carbons offer relatively low specific capacitance (< 200 F g^{-1}) in aqueous electrolytes because of their broad pore size distribution consisting of micropores (< 2 nm), mesopores (2–50 nm) and macropores (> 50 nm).[5] It is well known that the energy storage occurs primarily in micropores.[6-8] Nevertheless, activated carbons with very high micropore surface area still exhibit limited increase in electric double-layer capacitance, because it is difficult for inner pores to be fully accessed by electrolyte.[9-11] What is more, a sharp decrease in specific capacitance was observed at high current densities, because electrolyte transport is restricted at fast charge-discharge rates owing to the long-distance, tortuous and narrow pathway channels to the inner micropores.[12,13] Further research showed that the contribution of micropores to capacitance was dependent on the number of mesopores, which are important for the fast ion transport through the mesopores to micropores[14-17] and also help to enlarge the accessible surface for ions[18].For instance, porous carbons produced by pyrolysis of seaweeds with moderate surface area but tuned porosity (high proportion of micropores and a moderate amount of mesopores) were proved to be perfectly adapted for the formation of the electric double layer.[19] Micro/mesoporous carbons fabricated from KOH activation of ordered mesoporous carbons fully demonstrated that hierarchical pore structure and well-connected micro/mesopores were beneficial for fast ionic transportation within the mesopores and diffusion from mesopores to micropores, leading to high capacitance of 200 F g^{-1} and good rate performance in 6 M KOH.[20] Also, the work done by Kim and co-authors showed that a high mesopore/micropore ratio was more likely to ensure a high capacitance.[21] Recently, Wang *et al*. reported the preparation of three-dimensional graphene bubble network by a sugar-blowing approach.[22] The self-supported interconnected porous structure endowed such three-dimensional graphene with high capacitance of 250 F g^{-1} in 1 M H_2SO_4 and excellent rate capability (130 F g^{-1} at 100 A g^{-1}). Therefore, an appropriate proportion of mesopores, especially the interconnected mesopores, is very important for the achievement of high capacitance and excellent rate capability.

Recently, biomass-derived carbons have attracted much attention because of their outstanding electrochemical performance,[19,23-26] and also because biomass is an environmentally-friendly and renewable resource and often is low-cost.[27] Usually the wastes from natural sources, such as wood processing wastes, are burnt or just discarded. Therefore, it makes great sense to use them to produce high value-added products, such as carbon electrode materials for supercapacitors. Earlier studies showed that the activated carbons derived from wood presented moderate capacitance.[10,28] This may be resulted from the irregular particle shape and wide particle size distribution of the powder-type raw materials, which makes it difficult to control the gasification process and thus leads to wide pore size distribution and low micropore volume. Carbon in the form of fiber may be more effective to produce activated carbon with controllable high amounts of micropores on the surface, which will lead to narrowed pore size distribution and shortened transport distance for ions from electrolyte to micropores. Previous research showed that activated carbon fibers had a higher specific capacitance (vs. power-type activated carbons) due to the good accessibility of the electrolyte ions onto the electrode surface and low equivalent series resistance.[29] Therefore, activated wood-based carbon fibers may be promising electrode materials for high-performance supercapacitors. To the best of our knowledge, few papers have reported the fabrication of activated wood-based carbon fibers for supercapacitors. Furthermore, the effects of surface area, mesopore/micropore ratio and pore size on the capacitance and rate capability of the steam-wood-based activated carbons have not been comprehensively investigated.

In this work, a series of activated carbon fibers (ACFs) were fabricated by a simple one-step process involving carbonization and simultaneous activation of wood-based fibers which were derived from liquefied wood processing wastes. The effect of activation time on the microstructure, morphology, pore texture and surface area of the ACFs series was investigated in detail. Electrochemical measurements such as cyclic voltammetry measurement and galvanostatic charge/discharge test were conducted to evaluate the specific capacitance and rate capability of the ACFs series. The relationship between the structure and electrochemical performance was comprehensively discussed, giving a better understanding towards the wood-based activated carbons for high-performance supercapacitors

2 Experimental details

2.1 Chemicals

The waste wood shavings originated from fir (Cunninghamia lanceolata) were obtained from the furniture factory (Beijing, China). Phenol, hexamethylenetetramine, formaldehyde (CH_2O, 37wt% in water), hydrochloric acid (HCl, 37wt% in water), phosphoric acid (H_3PO_4, 37wt% in water) and sulphuric acid (H_2SO_4, 99wt% in water) were purchased from Beijing Chemical Plant. 1-Methyl-2-pyrrolidone (MP) and polyvinylidene fluoride (PVDF) were purchased from Alfa Aesar Corp. All the chemicals were used as received without further purification. Deionized water was used to wash the precursor fibers and prepare the electrolyte.

2.2 Synthesis of precursor fibers

In a typical procedure, the waste wood shavings were pulverized to a powder with the particle size in the range of 0.25–0.45 mm, and dried in an oven at 105 ^oC for 24 h before use. After that, 20 g of the dried wood powder was added into a 500 mL three-neck glass flask and mixed with a solution containing 80 g phenol and 6.4 g phosphoric acid. The mixture was heated up at a rate of 5 ^oC min^{-1} and kept at 160 ^oC for 2.5 h with continuous stirring and then the as-obtained mixture was purified using a sand-core filler funnel to obtain the phenol-liquefied wood. Subsequently, 10 g phenol-liquefied wood and 0.5 g hexamethylenetetramine were added into the feed box of a self-made spinning apparatus, and then heated up at a rate of 5 ^oC min^{-1} and kept at 175 ^oC for 20 min under vigorous stirring to prepare the spinning solution. Afterwards, the melt-spinning process was carried out at 125 ^oC. The resultant fibers were soaked in an acid solution that contains 7.4 mL formaldehyde, 6 mL hydrochloric acid and 1.4 mL deionized water and then cured at 90 ^oC for 2 h with a heating rate of 0.25 ^oC min^{-1}. Finally, the precursor fibers were obtained after being washed three times with deionized water and dried at 85 ^oC for 2 h.

2.3 Prepration of activated carbon fibers

A series of ACFs were fabricated by a simple one-step process of carbonization and water vapor activation with various activation time (20, 60, 100, 140, 180 and 220 min) from the as-prepared precursor fibers. For a typical preparation, about 5 g precursor fibers were put in a tube furnace and the carbonization/activation process was carried out at 850 ^oC (with a ramping rate of 4 °C min^{-1}) under steam/nitrogen mixture gas (the volume ratio of steam to nitrogen is ~0.38). The as-prepared ACFs were designated as ACFst, where t (20, 60, 100, 140, 180 and 220) represents the activation time.

2.4 Physical characterizations

The morphologies of the samples were characterized by a field emission scanning electron microscope (FESEM, Supra55, Carl Zeiss). X-ray Diffraction patterns were recorded by an X-ray diffractometer (XRD-6000, Shimadzu) with a Cu Kα radiation (wavelength 0.154 nm) at 40 kV and 30 mA. Nitrogen adsorption/desorption isotherms were collected at 77 K on an Autosorb-iQ (Quantachrome) automatic analyzer. The specific surface area was calculated by Brunauer–Emmett–Teller (BET) method. The micropore and mesopore surface areas were determined using t-Plot method. The total pore volume was based on the nitrogen adsorption volume at the maximum relative pressure. The micropore and mesopore volumes as well as pore size distribution were calculated using quenched solid density functional theory (QSDFT) method. To investigate the surface chemistry, X-ray photoelectron spectroscopy (XPS) measurements were performed on an ESCALAB 250Xi spectrometer (Thermo Fisher Scientific) using a monochromatic AlK α X-ray (1486.6 eV) source.

2.5 Electrochemical measurements

To prepare the electrodes, a mixture of the ACFs and PVDF binder with the weight percent ratio of 90:10 was dispersed in MP, and then the slurry was coated on the platinum current collectors. Afterwards, the electrodes were dried in a vacuum oven at 120 °C for 24 h. The loading mass of the active materials on each platinum plate was 2.1–2.5 mg cm^{-2}. Before testing, the working electrodes were immersed in the electrolyte for 24 h. The electrochemical measurements were firstly carried out in a three-electrode system with 1 M H_2SO_4 as electrolyte, an Ag/AgCl electrode as reference electrode and a slice of platinum plate as counter electrode. The potential window was between -0.1 and 0.9 V. Cyclic voltammetry (CV, at various scan rates from 20 to 100 mV s^{-1}) and electrochemical impedance spectroscopy (EIS, frequency from 10 mHz to 100 kHz) measurements were carried out on an electrochemical workstation (Autolab PGSTAT 302N, Metrohm, Netherlands). The galvanostatic charge/discharge processes were conducted on a LAND CT2001A battery tester (China) at different current densities from 0. 5 to 10 A g^{-1}. The specific capacitance, C_s (F g^{-1}), of the electrode material was calculated from the galvanostatic discharge results according to the following equation:

$C_s = i\Delta t/(m\Delta V)$

where I (A) refers to the discharge current, ΔV (V) represents the potential window within the discharge time Δt (s), and m (g) corresponds to the amount of active material on the electrode.

Then a sandwich-type capacitor based on ACFs180 was set up and tested using CV, galvanostatic charge/discharge, and EIS measurements. The two electrodes used in this sandwich-type capacitor had almost the same mass loading. Exceptionally, the CV tests were carried out on another electrochemical workstation (Potentiostat Model 263A, Princeton Applied Research). The capacitance, C (F g^{-1}), of ACFs180 from the CV curves was calculated by using the formula:

$C = 2\int idV/(m\Delta VS)$

where $\int idV$ is the integrated area under the CV curve, m (g) is the total mass of the active material on the two electrodes, ΔV (V) is the electrochemical window of the supercapacitor, and S (V s^{-1}) is the scan rate. The capacitance, C (F g^{-1}), was also calculated from the frequency response analysis, by $C = 1/(\pi m f Z'')$, where m (g) is the total mass of the active material on the two electrodes, f (Hz) is frequency and Z″ is the imaginary part of the impedance.

3 Results and discussion

3.1 Structure and morphology characterization

Fig. 1 shows the wide-angle XRD patterns of the ACFs series prepared by adjusting the carbonization/activation time. All the XRD patterns present two broad diffraction peaks (indicative of amorphous character) at around 20 and 43.5°, corresponding to the 002 and 101 reflections of graphitic carbon, respectively. Notably, the 101 diffraction peak decreases gradually from ACFs20 to ACFs220, suggesting the steady degradation of the carbon framework with the progress of gasification.

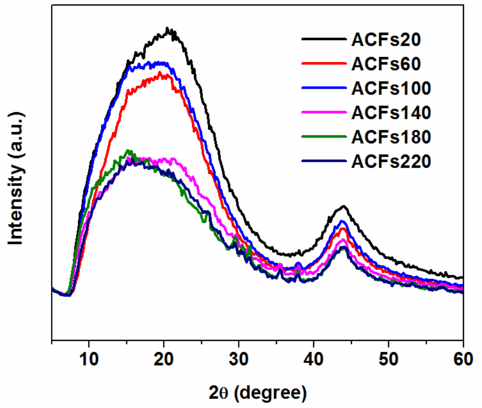

Fig. 1 XRD patterns of the ACFs series with different activation time.

The morphologies of the as-prepared ACFs series were characterized by SEM. As shown in Fig. 2, the ACFs series still show perfect fibrous morphorlog and a relatively smooth surface at low magnification. The average diameters of the ACFs series decrease with the progress of steam activaton due to the gasification of carbon.

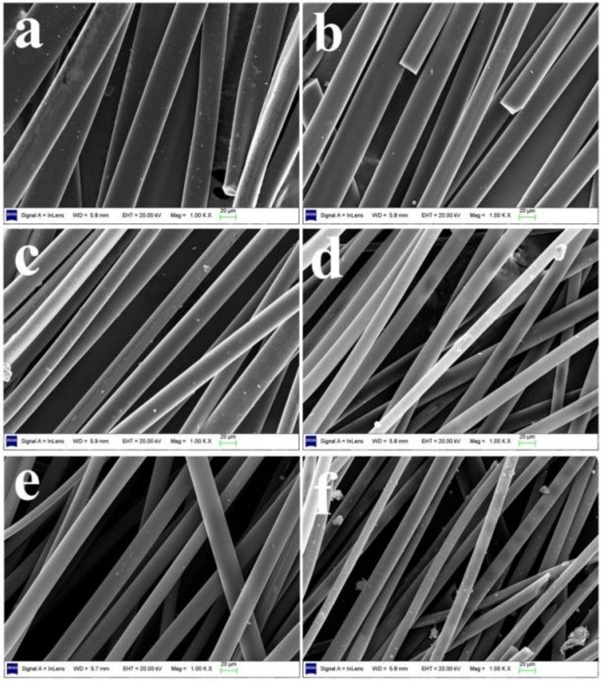

Fig. 2 SEM images of (a) ACFs20, (b) ACFs60, (c) ACFs100, (d) ACFs140, (e) ACFs180, and (f) ACFs220.

The porous structure of the ACFs series is quantitatively analyzed by nitrogen adsorption/desorption measurement. The nitrogen sorption isotherm of ACFs20 shows the type I curve with a sharp nitrogen adsorption taking place at the relative pressure below 0.1, indicative of a typical microporous structure.[30] As the activation time increases, the nitrogen sorption isotherm of the sample still roughly presents type I curve, but the knee in the isotherm becomes wider, suggesting the generation of mesopores and the broadening of pore size distribution.[31] In general, the size of micropores will become larger, and a certain proportion of micropores will enlarge into mesopores with the progress of steam gasification. The longer the activation time is, the larger the size of both micropores and mesepores as well as the volume of mesopores will be. Furthermore, big differences in the nitrogen uptake at low relative pressures (P/P_0 < 0.1), which indicates the relative volume of micropores, are observed. In detail, the nitrogen adsorption at a relative low pressure firstly increases with increasing the activation time to 180 min, then decreases when the activation time is further prolonged to 220 min. So it can be concluded that the activation time of 180 min is the optimal one which produces the largest volume of micropores, and the activation time of 220 min is too long, resulting in rapid enlargement of micropores into mesopores and severe degradation of carbon framework. As shown in Table 1, the sample fabricated using the shortest activation time (20 min) has the smallest mesopore volume of 0.164 cm^3 g^{-1} as well as the smallest micropore volume of 0.419 cm^3 g^{-1}. In contrast, the sample produced with longer activation time exhibits higher mesopore volume, and the mesopore volume reaches its maximum value of 0.935 cm^3 g^{-1} in ACFs220. On the other hand, the micropore volume and the total pore volume reach their maximum values of 0.862 and 1.686 cm^3 g^{-1}, respectively, in ACFs180. Fig. 3b shows the pore size distribution of the ACFs series calculated by the QSDFT method. Obviously, the size of micropores increases with the progress of gasification, mainly centering at 0.58 (ACFs20), 0.58 and 0.80 (ACFs60), 0.85 (ACFs100), 0.88 (ACFs140), 0.91 (ACFs180), and 0.96 (ACFs220) nm. The mesopores of ACFs20, ACFs60, ACFs100 and ACFs140 are in the range of 2–3 nm while it is in the range of 3–4 nm for ACFs180 and ACFs220. It is noteworthy that all the samples possess dramatically large specific surface area (> 1200 m^2 g^{-1}). Particularly, the specific and micropore surface areas reach as high as 3223 and 2300 m^2 g^{-1}, respectively, for ACFs180. The detailed parameters deduced from the nitrogen adsorption/desorption analysis for all the samples are listed in Table 1.

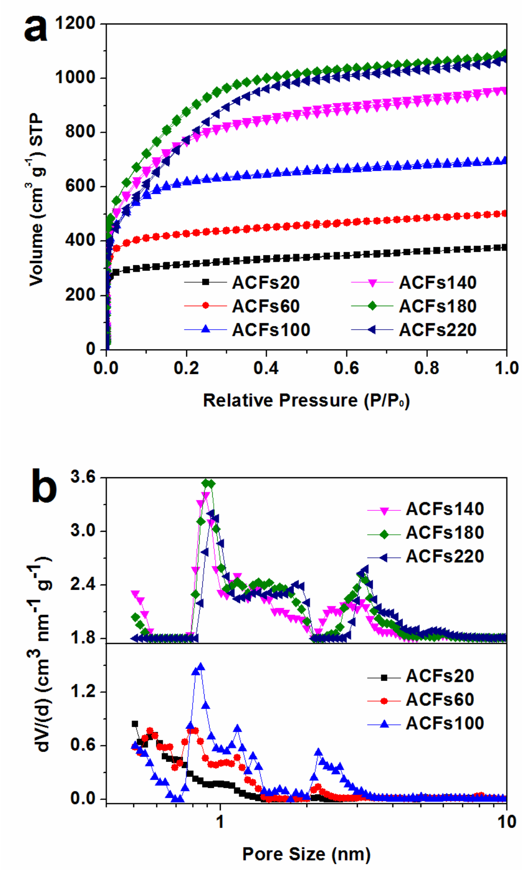

Fig. 3 (a) Nitrogen adsorption/desorption isotherms; (b) pore size distribution of the ACFs series. The pore size distribution curves of ACFs140, ACFs180 and ACFs220 are shifted vertically to make them easy to read.

Table 1 List of parameters deduced from nitrogen adsorption/desorption analysis for different materials[a]

Sample	S_{BET} (m^2 g^{-1})	S_{mic} (m^2 g^{-1})	S_{meso} (m^2 g^{-1})	V_t (cm^3 g^{-1})	V_{mic} (cm^3 g^{-1})	V_{meso} (cm^3 g^{-1})
ACFs20	1221	1041	180	0.583	0.419	0.164
ACFs60	1647	1422	225	0.775	0.549	0.226
ACFs100	2280	1996	284	1.073	0.612	0.461
ACFs140	2788	2120	668	1.482	0.724	0.758
ACFs180	3223	2300	923	1.686	0.862	0.824
ACFs220	2929	1389	1540	1.654	0.719	0.935

[a] S_{BET}: specific surface area; S_{mic}: micropore surface area; S_{meso}: mesopore surface area; V_t: total pore volume; V_{mic}: micropore volume; V_{meso}: mesopore volume.

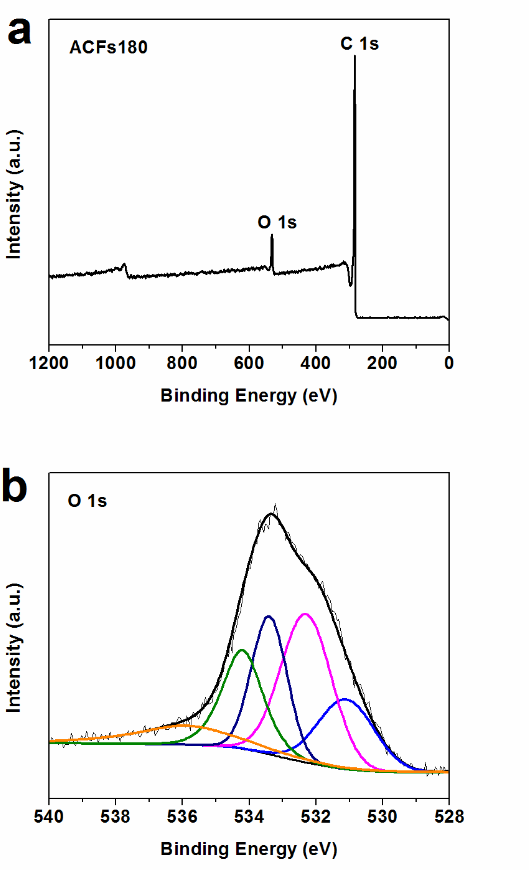

Fig. 4 (a) XPS survey spectrum of ACFs220 and (b) high-resolution XPS spectrum of O 1s peaks for ACFs180.

XPS analysis was conducted to estimate the superficial elemental composition and chemical structure of the ACFs series. Fig. 4 shows the XPS spectra of ACFs180. Although the spectra of only one sample are shown, the spectrum curves of all the samples are very similar. The XPS survey spectrum in Fig. 4a indicates the presence of oxygen species. According to XPS analysis, the percentage of oxygen was estimated to be 8.43, 8.37, 6.17, 6.28, 6.49 and 5.79 at.% for ACFs20, ACFs60, ACFs100, ACFs140, ACFs180 and ACFs220, respectively. The O species were further determined by XPS fine scanning. As displayed in Fig. 4b, the O 1s spectrum of ACFs180 was deconvoluted into five established groups: quinone (531.1 eV), C=O (532.3 eV), C–O (533.3 eV), C–OH (534.2 eV), and adsorbed H_2O (535.9 eV).[32] For comparison, the quantitative analyses of the oxygen species for all samples are listed in Table 2. No big difference in the relative surface concentration of oxygen species for the ACFs series is observed. It should be noted that there are a very small amount of nitrogen (< 0.5 at.%) and phosphorus (< 0.2 at.%) in the ACFs series.

Table 2 Relative surface concentration (%) of oxygen species obtained by fitting the O1s XPS spectra

Sample	531.1 eV	532.3 eV	533.3 eV	534.2 eV	535.9 eV
ACFs20	14	37	23	16	11
ACFs60	14	40	20	17	10
ACFs100	13	32	21	16	17
ACFs140	13	29	30	13	16
ACFs 180	17	33	22	19	10
ACFs 220	16	35	16	18	16

3.2 Electrochemical measurements

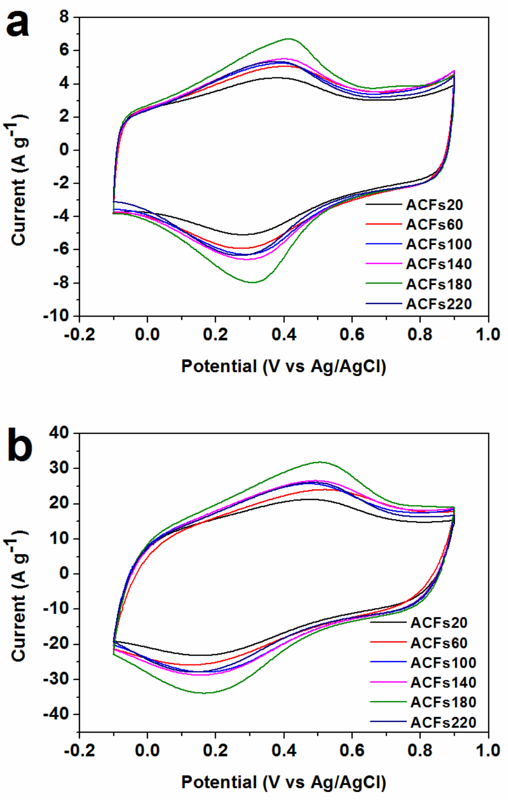

Fig. 5 CV curves of the ACFs series obtained at a scan rate of 20 (a) and (b) 100 (c) mV s^{-1}.

The electrochemical performance of the ACFs series was firstly evaluated using CV measurement. Fig. 5 shows the representative CV behaviors of the ACFs series in a three-electrode system in 1 M H_2SO_4 electrolyte. At the scan rate of 20 mV s^{-1}, all the samples demonstrate nearly rectangular-shaped CV curves with a few broad humps in these CV curves (Fig. 5a), owing to the combination effects of electric double-layer capacitance and pseudocapacitance. Herein, the redox peaks on the CV curves are mainly attributed to the reversible redox reactions of oxygen-containing groups.[33] In addition, although the nitrogen groups and phosphorus groups present in a small quantity, they also make some contribution to the total capacitance. The nitrogen groups bring about pseudocapacitance,[34] and the phosphorus groups enhance the electric double-layer capacitance.[35,36] Furthermore, the CV curve of ACFs180 has the largest loop area, indicative of the highest specific capacitance. As the scan rate increases to 100 mV s^{-1}, the rectangular-shaped CV curves (Fig. 5b) of the ACFs series only slightly distort, clearly showing good charge propagation and easy ion transport within the electrode materials.

Fig. 6 a and b show the galvanostatic charge/discharge profiles of the ACFs based electrodes at the current densities of 0.5 and 5 A g^{-1}, respectively. The galvanostatic charge/discharge profiles severely deviate from the linear curves below the voltage of 0.5 V due to the pseudofaradaic effect. There is no visible ohmic loss (IR drop) at the low current density, whereas high IR drop is observed at the higher current density of 5 A g^{-1} (Fig. 6b). As shown in Fig. 6b, the ACFs180 electrode demonstrates the minimal IR drop, indicating that the ACFs180 electrode material has very small resistance. Different current densities from 0.5 to 10 A g^{-1} were used to evaluate the rate capability of the samples. The specific capacitance as a function of current density is plotted in Fig. 6c. The specific capacitance values at 0.5 A g^{-1} for ACFs20, ACFs60, ACFs100, ACFs140, ACFs180 and ACFs220 are 218, 248, 254, 262, 280, and 242 F g^{-1}. It is worth noting that the specific capacitance of the ACFs180 electrode still reaches as high as 229 F g^{-1} at 10 A g^{-1}, corresponding to very high capacitance retention of 81.8% vs. that at 0.5 A g^{-1}. In order to clearly elucidate the high capacitive performance of the as-prepared ACFs, comparisons were performed with some reported representative carbons, including activated carbons, (ordered) mesoporous carbons, hierarchical porous carbons, and heteroatom-doped porous carbons (*e.g.* Nitrogen-doped porous carbons) (Table 3). To make meaningful comparisons, all the capacitance values are obtained using a three-electrode system with KOH or H_2SO_4 aqueous solution as electrolyte. Indeed, the capacitive performance achieved in this study is the most outstanding, even showing slightly higher specific capacitance than the N-doped high-surface-area carbons at the current density of 10 A g^{-1}.

Table 3 Comparison of the specific capacitance of the porous carbon materials in the literature

Materials	S_{BET} (m^2 g^{-1})	Electrolyte	C_s (F g^{-1})	Ref
Steam-activated carbons	1131	0.5 M H_2SO_4	142 (25 mV s^{-1})	10
Hierarchical porous carbons	2749	6 M KOH	223 (2 mV s^{-1})	15
KOH activated ordered mesoporous carbons	1410	6 M KOH	200 (0.5 A g^{-1})	20
Micro/mesoporous carbon nanospheres	3301	0.5 M H2SO4	219 (0.5 A g-1)	37
Nitrogen-doped porous carbons	1724	1 M H_2SO_4	220 (10 A g^{-1})	38
Activated carbon fibers	3223	1 M H_2SO_4	280 (0.5 A g^{-1})	This
			229 (10.0 A	work

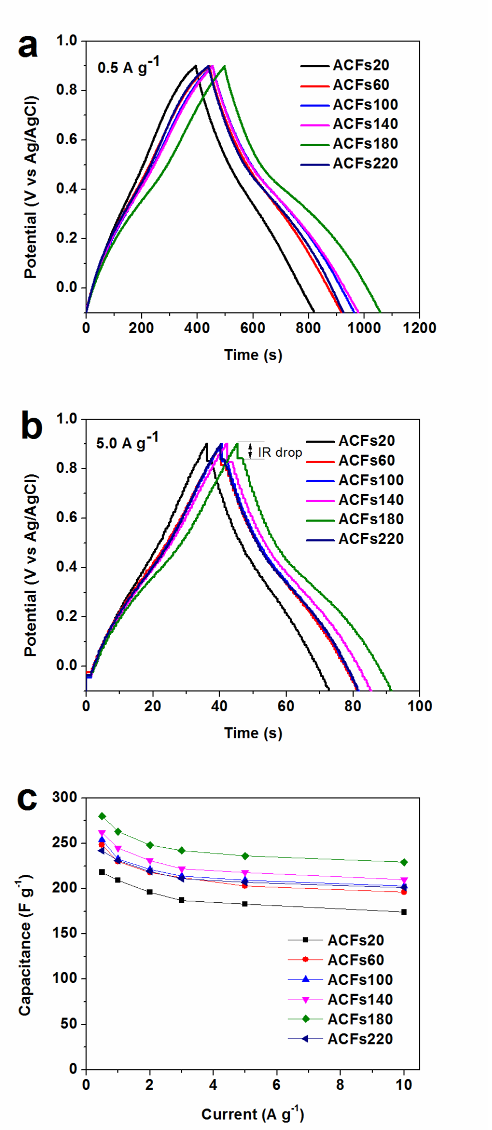

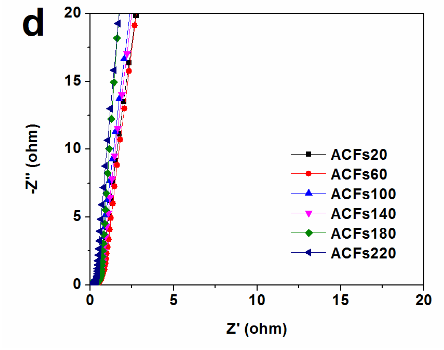

Fig. 6 Galvanostatic charge/discharge curves of the ACFs series at the current densities of (a) 0.5 and (b) 5.0 A g-1; (c) specific capacitance as a function of current density calculated from the galvanostatic charge/discharge curves; (d) Nyquist plots of the ACFs-based electrodes obtained in the frequency range from 100 kHz to 0.01 Hz.

In order to study the effect of the mesopore/micropore ratio on the rate capability of the activated carbons, the mesopore/micropore ratio as well as the capacitance retention as a function of activation time was plotted in Fig. 7. Roughly, the mesopore/micropore ratio and the capacitance retention follow the same trend. That is, the higher the mesopore/micropore ratio is, the better the rate capability will be. However, there are exceptions. For instance, ACFs20 and ACFs60 have similar mesopore/micropore ratio, but the capacitance retention of ACFs20 is slightly higher. This could be attributed to the larger surface area of ACFs60, resulting in more oxygen groups accessible to the electrolyte and thus leading to higher pseudocapacitance loss at high current densities. Also, the capacitance retention of ACFs180 is higher than that of ACFs140, though the mesopore/micropore ratio decreases at the activation time of 180 min. This may be related to the size of mesopores and the status of the mesopores in the carbon frame work. It is believed that an appropriate proportion of mesopores, especially interconnected mesopores, in the range of 3–4 nm is very important for high capacitance and excellent rate performance.[15,19] Furthermore, we can see from Fig. 7 that the increase in capacitance retention for ACFs180 and ACFs220 is faster than those of the other samples, conforming that the mesopore structure of ACFs180 and ACFs220 is more beneficial to the achievement of high capacitive performance. Hence, there may two factors leading to higher capacitance retention for ACFs180 and ACFs220: (I) the size of their mesopores is larger just in the range of 3–4 nm; (II) longer activation time may give rise to more mesopores that are connected reciprocally.

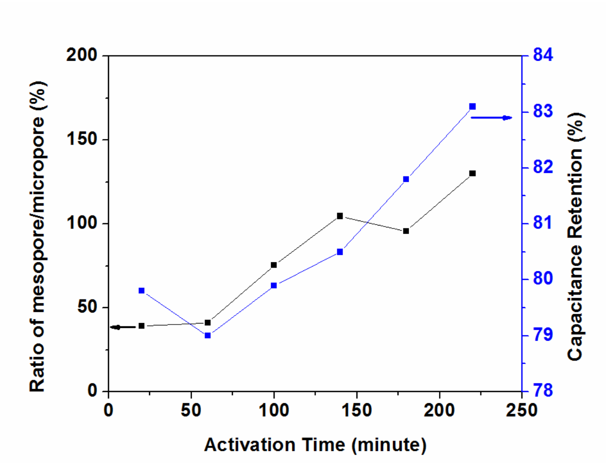

Fig. 7 The mesopore/micropore ratio and capacitance retention of the ACFs series versus the activation time.

The Nyquist plots from the EIS measurement further reveal the ion transport kinetics at the electrode/electrolyte interface, which can qualitatively demonstrate the formation rate of the electric double layer and further verify the role of the mesopores. In general, the larger the slop the faster the electric double layer will be formed.[39] As displayed in Fig. 6d, the slop for ACFs180 and ACFs220 is apparently much larger than those of the other samples, indicative of fast ion transport due to the presence of mesopores in the range of 3–4 nm. Furthermore, all the electrodes show small equivalent series resistance (0.72–0.78 Ω) and charge transfer resistance (0.21–0.35 Ω), which are important for high rate performance.

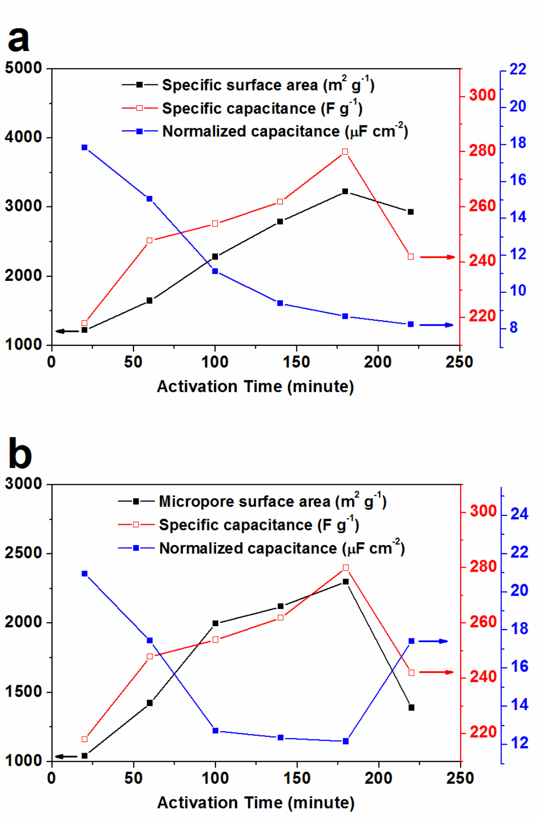

Fig. 8 (a) Specific surface area, specific capacitance and specific capacitance normalized by specific surface area versus activation time; (b) micropore surface, specific capacitance area and specific capacitance normalized by micropore surface area versus activation time. In order to clearly elucidate the specific capacitance is more closely related to micropore surface area, the specific capacitance as a function of activation time is plotted in both figures.

In order to investigate the effects of activation time and pore texture on the capacitance of the activated carbons, specific surface area, micropore surface area, specific capacitance, and normalized capacitance by specific surface area and micropore surface area are plotted as a function of activation time (Fig. 8). As shown in Fig. 8a, the specific capacitance normalized by specific surface area decreases with increase of activation time, though the specific surface area decreases at the activation time of 220 min. This indicates that the mesopore surface area makes limited contributions to the total capacitance. We can see that the trend of the specific capacitance is more close to that of micropore surface area (Fig. 8b), rather than that of specific surface area. More interestingly, the specific capacitances normalized by micropore surface area for ACFs60 and ACFs220 have almost the same value (17.44 and 17.42 μF cm^{-2}, respectively). This means that the mesopore surface area or mesopores offer negligible capacitance. Thus, it can be concluded that the specific capacitance is directly related to the micropore surface area. On the other hand, the normalized capacitance by micropore surface area for ACFs20 is 20% higher than that of ACFs60, though the micropore surface area of ACFs60 is 36% larger than that of ACFs20. According to the literature,[6,40] pore size that very close to the ion size seems to give rise to the maximum capacitance. In this case, ACFs20 has more ultramicropores (< 0.6 nm) than any other sample, and thus could offer higher capacitance per unit area. Furthermore, it seems that micropores with a size of more than 0.6 nm may have similar electric double-layer behavior, as is expressed by the similar normalized capacitance by micropore surface area for ACFs60 and ACFs220. Indeed, Stoeckli et al. reported that the surface-related capacitance (F m^{-2}) in the 1–2 M H_2SO_4 is practically independent of the micropore width when the pore width of micropores is between 0.7 and 1.8 nm.[41] In addition, we can see that the decrease of the normalized capacitance by micropore surface area becomes slower and slower from ACFs100 to ACFs180. This can be owed to the increase of mesopores as well as mesopore size from ACFs100 to ACFs180. Thus, an appropriate proportion of mesopores with appropriate pore size is really very important for the accessibility of the inner micropores to the electrolyte, which ensures the achievement of high capacitance.

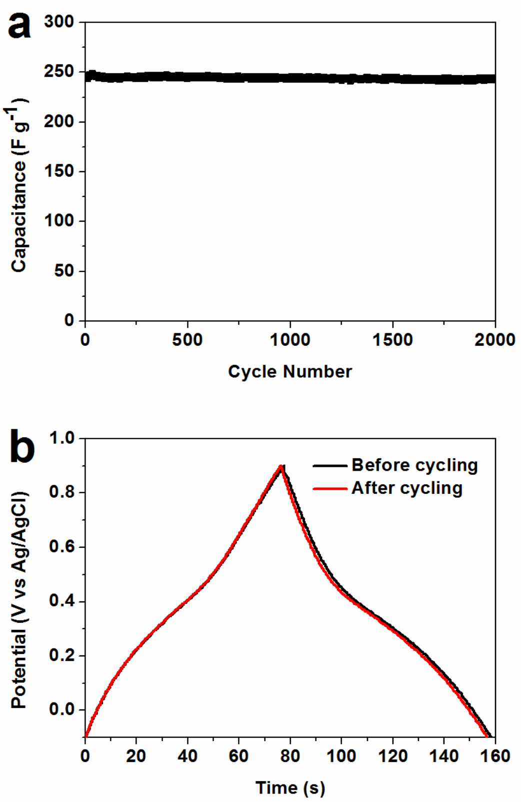

Fig. 9 (a) Cyclic stability of the ACFs180 electrode in 1 M H_2SO_4 (current density of 3 A g^{-1}) and (b) galvanostatic charge/discharge curves of the ACFs180 electrode before and after the 2000 cycles.

The cyclic stability of the electrode materials is another key issue for the practical application; therefore, the galvanostatic charge/discharge test was performed to evaluate the stability of the ACFs180 electrode in 1 M H_2SO_4 under the current density of 3 A g^{-1}. As shown in Fig. 9a, the ACFs180 electrode exhibits good long-term cyclic stability, maintaining 99.3% of its original capacitance (a decrease from 244.8 to 243.1 F g^{-1}) after 2000 cycles. Fig. 9b shows the galvanostatic charge/discharge curves of the first and last cycles, demonstrating no obvious difference which confirms the excellent stability of the ACFs180 electrode material.

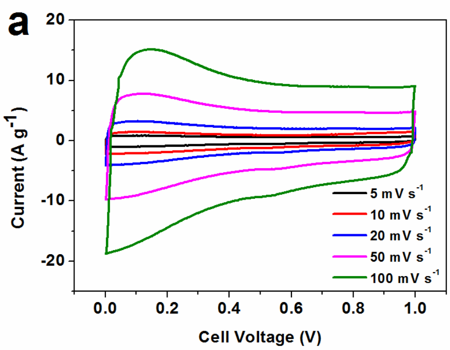

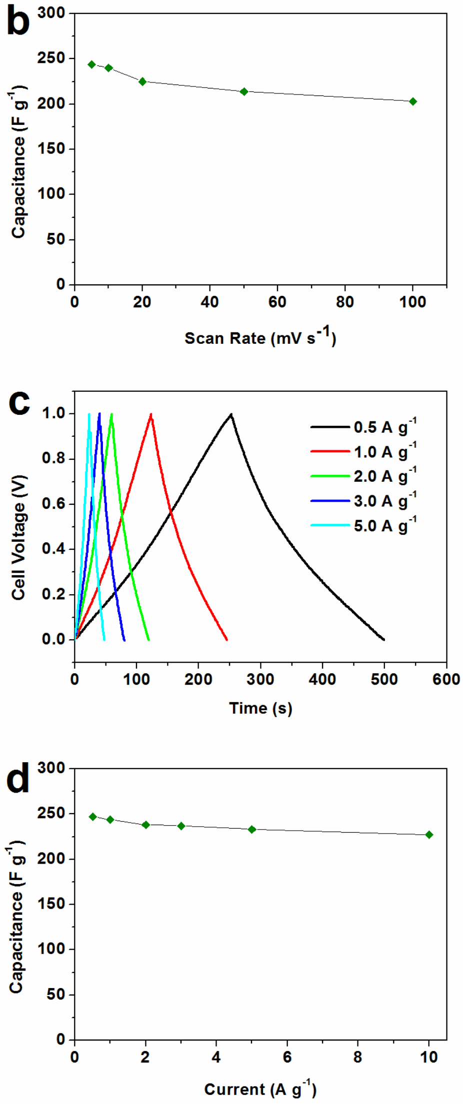

Fig. 10 Electrochemical measurements measured in a two-electrode symmetrical supercapacitor on the basis of ACFs180: (a) CV curves at different scan rates ranging from 5 to 100 mV s^{-1}; (b) specific capacitance as a function of the scan rate; (c) galvanostatic charge/discharge curves at various current densities between 0.5 and 10 A g^{-1}; (d) specific capacitance with the current density.

In order to determine the true performance of the as-prepared materials, we constructed and measured the performance of a two-electrode symmetrical supercapacitor on the basis of ACFs180. Fig. 10a presents the CV curves of the two-electrode symmetrical supercapacitor at different scan rates ranging from 5 to 100 mV s^{-1}. It shows a big broad peak in the low potential region and a nearly rectangular background. The capacitance deduced from the CV curves shows little changes in the range of scan rates. As shown in Fig. 10b, it slowly decreases from 244 F g^{-1} at 5 mV s^{-1} to 203 F g^{-1} at 100 mV s^{-1}. Fig. 10c exhibits the charge/discharge profiles. The IR drop only slowly increases as the current density increases, clearly showing good conductivity of ACFs180. As shown in Fig. 10d, the capacitance calculated from the discharge profile at 0.5 A g^{-1} is

247 F g^{-1} and still maintains 227 F g^{-1} at 10 A g^{-1}, corresponding to 91.9% capacitance retention. These results indicate that ACFs180 is a promising electrode material for high-performance supercapacitors.

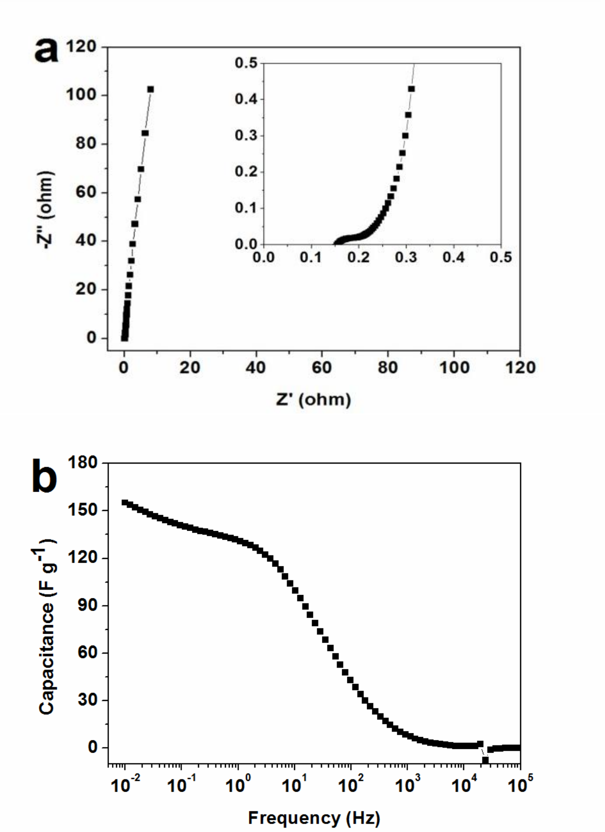

Fig. 11 (a) Nyquist plot for the ACFs electrodes in in a two-electrode symmetrical supercapacitor, and the inset shows the magnified high-frequency region. (b) Frequency response of the specific capacitance of the ACFs180 electrode.

The Nyquist plot in Fig. 11a shows that the equivalent series resistance and charge transfer resistance are very small, which to some extent explains the good rate performance of ACFs180. Furthermore, the vertical line in the low-frequency region indicates nearly ideal capacitor behavior of the ACFs180 electrode. The capacitance from the EIS data as a function of frequency is shown in Fig. 11b. The capacitance at 0.01 Hz is 154 F g^{-1} and then decreases sharply at around 2 Hz, which is a common feature for porous carbon electrodes because the deep inner pores cannot be accessed by the electrolyte ions at high frequency, thus leading to a sharp decrease in capacitance. However, the capacitance still remains 99 F g^{-1} at 10 Hz, over 64% of the maximum capacitance at the frequency of 0.01 Hz, indicating fast ion transport and adsorption on the electrode surface.[42]

Conclusions

A series of ACFs with different levels of burn-off were successfully prepared by an easy one-step process of carbonization and activation of wood-derived fibers. The porosity, especially the mesopore/micropore ratio, could be easily tuned by controlling the activation time. And the micropore and mesopore surface areas were effectively increased with the progress of gasification before excessive burn-off occurred at the activation time of 220 min. The specific capacitance of the ACFs electrodes was directly related to the micropore surface area, and the micropres with a size greater than 0.6 nm seem to contribute equally to the electric double layer capacitance. Furthermore, an appropriate proportion of mesopores with a reasonable size (e.g. 3–4 nm) was very important to ensure the achievement of both high capacitance and excellent rate capability. ACFs180 with the highest micropore surface area and a relatively high proportion of mesopores in the range of 3–4 nm presented the highest specific capacitance (280 F g^{-1}) as well as excellent rate performance. In addition, the ACFs180 electrode exhibited good cyclic stability during the 2000 charge/discharge cycles, making it a promising electrode material for high-performance supercapacitors.

Acknowledgements

The authors are grateful for the financial supports from the Special Research Funds of the Forestry Industry for the Public Welfare of China (No. 201004057), National Natural Science Foundation of China (Nos. 51072013, 51272021, 51142004) and Natural Science Foundation of Jiangsu Province (BK20131147).

Notes and references

[a] College of Materials Science and Technology, Beijing Forestry University, Beijing 100083 (China). Tel: +8610-62337751; Email: Zhaows@bifu.edu.cn.

[b] State Key Laboratory of Organic-inorganic Composite, Beijing University of Chemical Technology, Beijing 100029 (China). Fax: +8610-64412084; Tel: 8610-64412084; E-mail: yuyh@mail.buct.edu.cn.

† These authors contributed equally to this work.

1 P. Simon and Y. Gogotsi, *Nat. Mater.*, 2008, 7, 845–853.
2 Y. Zhu, S. Murali, M. D. Stoller, K. J. Ganesh, W. Cai, P. J. Ferreira, A. Piekle, R. M. Wallace, K. A. Cychosz, M. Thommes, D. Su, E. A. Stach and R. S. Ruoff, *Science*, 2011, 332, 1537–1541.
3 L. -Q. Mai, A. Minhas-Khan, X. Tian, K. M. Hercule, Y. -L. Zhao, X. Lin and X. Xu, Nat. Commun., 2013, 4, 2923–2929.
4 S. Bose, T. Kuila, A. K. Mishra, R. Rajasekar, N. H. Kim and J. H. Lee, J. Mater. Chem., 2012, 22, 767–784.
5 L. L. Zhang and X. S. Zhao, Chem. Soc. Rev., 2009, 38, 2520–2531.
6 J. Chmiola, G. Yushin, Y. Gogotsi, C. Portet, P. Simon and P. L. Taberna, Science, 2006, 313, 1760–1763.
7 D. -W. Wang, F. Li, M. Liu, G. Q. Lu and H. -M. Cheng, Angew. Chem. lnt. Ed., 2008, 47, 373–376.
8 C. Ma, Y. Song, J. Shi, D. Zhang, X. Zhai, M. Zhong, Q. Guo and L. Liu, Carbon, 2013, 51, 290–300.
9 H. Teng and C. -T. Hsieh, Ind. Eng. Chem. Res., 1998, 37, 3618–3624.
10 F. -C. Wu, R. -L. Tseng, C. -C. Hu and C. -C. Wang, J. Power Source, 2004, 138, 351–359.
11 C. Vix-Guterl, E. Frackowiak, K. Jurewicz, M. Friebe, J. Parmentier and F. Béguin, Carbon, 2005, 43, 1293–1302.
12 H. Teng, Y. -J. Chang and C. -T. Hsieh, Carbon, 2001, 39, 1981–1987.

13 D. -D. Zhou, Y. -J. Du, Y. -F. Song, Y. -G. Wang, C. -X. Wang and Y. -Y. Xia, J. Mater. Chem. A, 2013, 1, 1192–1200.

14 E. Frackowiak, G. Lota, J. Machnikowski, C. Vix-Guterl and F. Béguin, Electrochim. Acta, 2006, 51, 2209–2214.

15 K. Xia, Q. Gao, J. Jiang and J. Hu, Carbon, 2008, 46, 1718–1726.

16 T. E. Rufford, D. Hulicova-Jurcakova, Z. Zhu and G. Q. Lu, J. Phys. Chem. C, 2009, 113, 19335–19343.

17 W. -Y. Tsai, P. -C. Gao, B. Daffos, P. -L. Taberna, C. R. Perez, Y. Gogotsi, F. Favier and P. Simon, Electrochem. Commun., 2013, 34, 109–112.

18 Z. –S. Wu, Y. Sun, Y. –Z. Tan, S. Yang, X. Feng and K. Müllen, *J. Am. Chem. Soc.*, 2012, 134, 19532–19535.

19 E. Raymundo-Piñero, M. Cadek and F. Béguin, Adv. Funct. Mater., 2009, 19, 1032–1039.

20 Y. Lv, F. Zhang, Y. Dou, Y. Zhai, J. Wang, H. Liu, Y. Xia, B. Tu and D. Zhao, J. Mater. Chem., 2012, 22, 93–99.

21 K. -S. Kim and S. -J. Park, J. Power Source, 2013, 244, 792–798.

22 X. Wang, Y. Zhang, C. Zhi, X. Wang, D. Tang, Y. Xu, Q. Weng, X. Jiang, M. Mitome, D. Golberg and Y. Bando, Nat. Commun., 2013, 4, 2905–2911.

23 E. Raymundo-Piñero, F. Leroux and F. Béguin, Adv. Mater., 2006, 18, 1877–1882.

24 C. Peng, X. -B. Yan, R. -T. Wang, J. -W. Lang, Y. -J. Ou and Q. -J. Xue, Electrochim. Acta, 2013, 87, 401–408.

25 M. Biswal, A. Banerjee, M. Deo and S. Ogale, Energy Environ. Sci., 2013, 6, 1249–1259.

26 W. Qian, F. Sun, Y. Xu, L. Qiu, C. Liu, S. Wang and F. Yan, Energy Environ. Sci., 2014, 7, 379–386.

27 B. Hu, K. Wang, L. Wu, S. -H. Yu, M. Antonietti and M. -M. Titirici, Adv. Mater., 2010, 22, 813–828.

28 F. -C. Wu, R. -L. Tseng, C. -C. Hu and C. -C. Wang, J. Power Sources, 2005, 144, 302–309.

29 M. Endo, Y. J. Kim, T. Maeda, K. Koshiba, K. Katayam and M. S. Dresselhaus, *J. Mater. Res.*, 2001, 16, 3402–3410.

30 M. Kunowsky, A. Garcia-Gomez, V. Barranco, J. M. Rojo, J. Ibañez, J. D. Carruthers and A. Linares-Solano, Carbon, 2014, 68, 553–562.

31 W. Gu, M. Sevilla, A. Magasinski, A. B. Fuertes and G. Yushin, Energy Environ. Sci., 2013, 6, 2465–2476.

32 R. Arrigo, M. Havecker, S. Wrabetz, R. Blume, M. Lerch, J. McGregor, E. P. J. Parrott, J. A. Zeitler, L. F. Gladden, A. Knop-Gericke, R. Schlogl and D. S. Su, J. Am. Chem. Soc., 2010, 132, 9616–9630.

33 D. -W. Wang, F. Li, J. Zhao, W. Ren, Z. -G. Chen, J. Tan, Z. -S. Wu, L. Gentle, G. Q. Lu and H. -M. Cheng, ACS Nano, 2009, 3, 1745–1751.

34 Z. -S. Wu, A. Winter, L. Chen, Y. Sun, A. turchanin, X. Feng and K. Müllen. Adv. Mater., 2012, 24, 5130–5135.

35 X. Yan, Y. Liu, X. Fan, X. Jia, Y. Yu and X. Yang. J. Power Sources, 2014, 248, 745–751.

36 X. Yan, Y. Yun and X. Yang. RSC Adv**.**, 2014, DOI: 10.1039/C4RA02299H.

37 D. Tashima, E. Yamamoto, N. Kai, D. Fujikawa, G. Sakai, M. Otsubo and T. Kijima, Carbon, 2011, 49, 4848–4857.

38 L. Hao, B. Luo, X. Li, M. Jin, Y. Fang, Z. Tang, Y. Jia, M. Liang, A. Thomas, J. Yang and L. Zhi, Energy Environ. Sci., 2012, 5, 9747–9571.

39 F. M. Hassan, V. Chabot, J. Li, B. K. Kim, L.Ricardez-Sandoval and A. Yu, J. Mater. Chem. A, 2013, 1, 2904–2912.

40 C. Largeot, C. Portet, J. Chmiola, P. -Louis. Taberna, Y. Gogotsi and P. Simon, J. Am. Chem. Soc., 2008, 130, 2730–2731.

41 F. Stoeckli and T. A. Centeno, J. Mater. Chem. A, 2013, 1, 6865–6873.

42 Z. Chen, J. Wen, C. Yan, L. Rice, H. Sohn, M. Shen, M. Cai, B. Dunn and Y. Lu, Adv. Energy Mater., 2011, 1, 551–556.